

# Mechanical Behavior of Alumina/Poly(methyl methacrylate) Nanocomposites

Benjamin J. Ash,\* Richard W. Siegel, and Linda S. Schadler

Materials Science and Engineering Department and Rensselaer Nanotechnology Center, Rensselaer Polytechnic Institute, Troy, New York 12180

Received September 24, 2003; Revised Manuscript Received December 15, 2003

**ABSTRACT:** Alumina/poly(methyl methacrylate) (PMMA) nanocomposites were synthesized using 38 and 17 nm alumina nanoparticles. At an optimum weight fraction, the resulting nanocomposites display a room-temperature brittle-to-ductile transition in uniaxial tension with an increase in the strain-to-failure that averages 40% strain and the appearance of a well-defined yield point in uniaxial tension. Concurrently, the glass transition temperature ( $T_g$ ) of the nanocomposites drops by more than 20 °C. The brittle-to-ductile transition is found to depend on poor interfacial adhesion between polymer and nanoparticle. This allows the nucleation of voids, typically by larger particles (~100 nm), which subsequently expand during loading. This void formation suppresses craze formation and promotes delocalized shear yielding. In addition, the reduction in  $T_g$  shrinks the shear yield envelope, further promoting this type of yield behavior. The brittle-to-ductile phenomenon is found to require both larger particles for void growth and smaller particles that induce the lowering of yield stress.

## Introduction

Traditional polymer composites filled with micrometer-size fillers often show improvements in their mechanical properties in the form of increases in modulus, yield strength, and glass transition temperature.<sup>1,2</sup> However, these gains are usually accompanied by losses in ductility and toughness. In addition, large amounts of filler are often required to achieve the desired properties, often diminishing the weight savings gained in using low-density polymers. Polymer nanocomposites have been shown to provide unique combinations of mechanical and thermal properties often at very low filler weight fractions. For example, Sumita et al. found dramatic improvements in the yield stress (30%) and Young's modulus (170%) in nanofilled polypropylene compared to micrometer-filled polypropylene.<sup>3</sup> These composites also showed no decrease in the stain-to-failure when filled with silica ranging from 7 to 40 nm in diameter. Similarly, Ou et al. filled nylon-6 with 50 nm silica particles and reported increases in tensile strength (15%), strain-to-failure (150%), Young's modulus (23%), and impact strength (78%) with only 5 wt % nanoparticles.<sup>4</sup> In a rubbery polyurethane elastomer, Petrovic and Zhang<sup>5</sup> found that a 6-fold increase in the elongation-at-break and a 3-fold increase in the modulus were achievable with 40 wt % 12 nm silica compared to a micrometer-sized filler that embrittled the polymer. Furthermore, the nanocomposites showed no reduction in transparency even at these relatively high loadings unlike the micrometer-sized filled systems.

The dramatic changes in mechanical properties observed in nanofillers challenge existing theories of mechanical reinforcement. Paramount to understanding nanocomposite behavior is addressing the presence of a large volume fraction of an "interphase zone" (IZ) that has properties different from the bulk polymer. The IZ is defined as the region surrounding each particle where

the polymer chain dynamics may be altered due to intimate contact with the nanoparticles (resulting in restricted or enhanced mobility) and this immediate layer's "far-field" influence on the surrounding matrix. Because of the relatively large volume fraction of interfacial polymer in even moderately filled nanocomposites, this IZ could occupy a considerable volume fraction in the composite. Modeling the IZ is difficult as imperfect bonding, mechanical stresses, and chemical interactions can all play a decisive role in determining its behavior. Ji et al.<sup>6</sup> recently modified Takayangi's two-phase model<sup>7</sup> to incorporate the interphase zone and were able to successfully reproduce the increases in the modulus of a clay/nylon-6 nanocomposite system. Their treatment modeled the interphase zone as a linear gradient change in the modulus between the surface of the filler and the matrix and introduced the critical effect of particle size (through the increase in volume fraction of the interphase) into the theory. The curves predicted by the model were shown to be in good agreement with the experimental results.

In addition to the IZ, the presence of fillers alone can also affect the bulk mechanical properties of a polymer matrix by altering the local stress state. In rubber-filled epoxies, Lazzeri and Bucknall show that a stress, either externally applied or resulting from differences in thermal expansion coefficient upon specimen cooling, can induce microvoid formation in lower modulus rubber particles through cavitation.<sup>8</sup> The cavities relieve the triaxial stress state present in the matrix, inhibiting bulk polymer void formation and subsequent crazing, and promoting shear and other forms of energy dissipating yield phenomena resulting in a tougher material.<sup>9</sup> In high impact polystyrene, dispersed rubber particles can initiate microcrazing throughout the matrix, increasing the overall toughness of the composite, although particles less than 1  $\mu\text{m}$  in diameter did not serve to initiate crazes and thus did not toughen the matrix.<sup>10</sup> The loadings required to provide the enhanced fracture toughness, however, are on the order of 40–50 vol % rubber, resulting in dramatic reductions in the

\* To whom correspondence should be addressed. E-mail: bjaash@sandia.gov; Current address: Sandia National Laboratories, PO Box 5800, Albuquerque, NM 87185-0958.

modulus of the resulting composite. Jansen et al.<sup>11</sup> found that a transformation from brittle to ductile behavior could be achieved in rubber-toughened PMMA when the size of the rubber regions (lightly cross-linked epoxy) was reduced to between 70 and 30 nm. These composites showed major improvements in the strain-to-failure with typical extensions of between 110% and 130% strain. However, because the rubber loading was still upward of 30%, a major drop in the yield strength of 50–60% was observed.

Enhanced toughness in nanocomposites has also been predicted to result from a critical interparticle spacing.<sup>12</sup> Wu hypothesized that if neighboring particles' stress fields overlap, there exists a critical ligament thickness that will result in a toughening of the matrix due to stress field interactions.<sup>12</sup> This concept has since been used to describe the changes in mechanical properties in rubber filled epoxy, nanosilica filled nylon-6, and nanosilica filled PMMA–HEMA.<sup>1,8,13,14</sup> Toughness is thus achieved when a large volume of the bulk composite has its stress state altered by the filler, favoring more energy-absorbing yielding mechanisms. Pearson and Yee also noted an increase in the fracture toughness of rubber modified epoxies with decreasing particle size<sup>15</sup> leading to smaller interparticle distances and a reduction in the volume of filler needed to toughen the composite. Thus, the affected volume is greatly enhanced through the use of the nanoparticle fillers.

A critical parameter in controlling the mechanical properties of any nanocomposite is the dispersion state of the nanoparticles. Since these high surface area fillers tend to aggregate, silanes and organotitanates are used extensively both to tailor the particle surface properties to mimic the surrounding matrix and to lower their surface energy, thereby reducing their tendency to agglomerate.<sup>16–18</sup> Other methods to alter the surface properties of the nanoparticles include radiation grafting,<sup>19</sup> chemical vapor deposition, and a host of complicated synthesis procedures that attempt to polymerize polymer chains off of initiating agents coupled to the surface.<sup>20–22</sup> In addition to achieving better dispersion, these techniques ultimately control the very nature of the IZ, which can define the resulting composite properties. The deliberate tailoring of the polymer–particle interface results in the ability to alter the properties of the entire matrix through the addition of a few volume percent of nanoparticles. Most often, though, the interface between particle and polymer is made stronger, and the special case where the interface is weakened has been largely neglected. Thus, the special case of a weak interface receives particular attention in the current research.

The incorporation of nanoparticles into polymeric matrices often has entirely unexpected results directly related to the interaction between particle and polymer. The present work focuses on the evaluation of the thermal and mechanical properties of alumina/PMMA nanocomposites through the use of uniaxial tensile testing, electron microscopy, X-ray scattering, and differential scanning calorimetry. Specifically, the goal of the present work was to synthesize and characterize nanocomposites where the interface between particle and polymer is very weak, with poor wetting of the particle to the polymer, and to subsequently evaluate their thermal and mechanical properties. The converse problem, a strong interfacial bond between particle and polymer, has already been evaluated in the literature

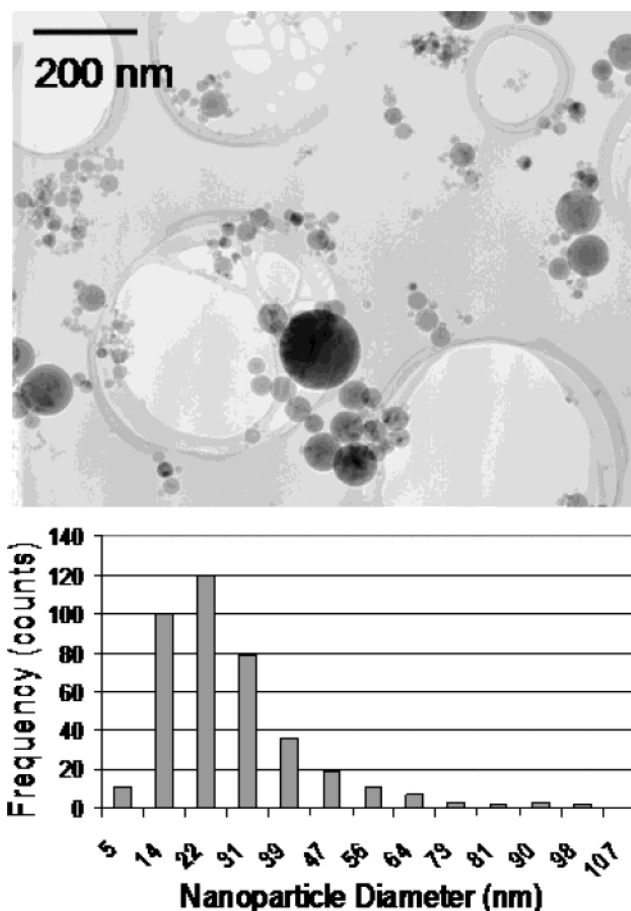


**Figure 1.** TEM micrograph of 38 nm alumina nanoparticles on a holey carbon TEM grid. Below: Nanoparticle size distribution.

as discussed above. The present work is an extension of previous work conducted with 39 nm alumina and PMMA.<sup>23,24</sup>

## Experimental Section

**General Information.** Nanocrystalline, spherical alumina ( $\gamma$ - $\text{Al}_2\text{O}_3$ ,  $\rho = 3.6 \text{ g cm}^{-3}$ ) with a reported mean diameter of 38 nm and specific surface area of  $44 \text{ m}^2/\text{gram}$  was obtained from Nanophase Technologies Corp. (NTC). The particle size was determined through BET gas adsorption by NTC. The particles have a relatively broad size distribution as shown in the transmission electron microscope (TEM) micrograph of Figure 1. Analysis of this image resulted in the distribution of particle sizes shown in Figure 1 (inset) with a mode of 28 nm and a median particle size of 60 nm. 17 nm diameter alumina was purchased from Nanotechnologies, Inc. and had a reported specific surface area of  $98 \text{ m}^2/\text{gram}$  (also by BET). Micrometer-sized alumina ( $\gamma$ - $\text{Al}_2\text{O}_3$ ,  $< 10 \mu\text{m}$ ) was obtained through Aldrich Chemical Co. Subsequent TEM analysis of this micrometer-sized alumina showed that it was composed of micrometer-sized aggregates of nanoscale, platelet-like particles.

Methyl methacrylate (MMA) (99% stabilized with 100 ppm MEHQ, Acros), 1-decanethiol (96% Aldrich), methacrylic acid (MAA) (99% Aldrich), and 3-glycidioxypropyltrimethoxysilane (GPS) (96% Gelest, Inc.) were used without further purification. 2,2-Azobis(isobutyronitrile) (AIBN) (98% Aldrich) was dissolved, filtered, and recrystallized from methanol. Reagent grade toluene was dried over  $\text{CaH}_2$  and distilled immediately prior to use.

**Nanoparticle Coating.** The nanoalumina was coated similarly to the procedure found in Tsubokawa et al.<sup>25</sup> In general, 5 g of nanoparticles were dried in a vacuum oven ( $195^\circ\text{C}$ ) for 24 h and then dispersed in 150 mL dry toluene with the aid of an ultrasonic probe. Following sonication of the

**Table 1. Physical Characterization of Polymerized Neat PMMA and Nanocomposites**

	$M_n$	PDI
neat PMMA	144 000	1.5
neat PMMA with added MAA	156 000	1.4
2.2 wt % 38 nm as-received alumina (no MAA)	152 000	1.6
2.2 wt % 38 nm alumina with added MAA	150 000	1.5

particles, the particle/toluene slurry was added to a 250 mL round-bottom flask charged with a stir bar, and a 5% v/v GPS/toluene solution was added dropwise with stirring. The amount of silane coupling agent was determined based on the reported specific surface area of the particles, the number of surface hydroxyls present on the surface of  $\gamma$ -alumina ( $5\text{--}10\ \mu\text{mol m}^{-2}$ ),<sup>26</sup> and the molecular weight of the particular silane to be used. The mixture was then heated to reflux and allowed to react for 20 h under dry nitrogen. Afterward, the mixture was allowed to cool and the resulting slurry was centrifuged for 3 min at 3000 rpm and the toluene decanted. The particles were washed with 100 mL of toluene and centrifuged/washed twice to ensure no unreacted silane remained.

The particles were dried in a vacuum oven at room temperature for a period of 24 h. The presence of the silane on the surface of the particles was confirmed by Fourier transform infrared spectroscopy (FTIR). Thermal gravimetric analysis (TGA) was also performed on the powders both before drying, after drying, and after coating to further prove the existence of the silane adsorbed/attached to the particle surface. This analysis was carried out on a Mettler-Toledo TGA/SDTA851e/LF1100/MT5/498 from 50 to 1000 °C at 20 °C min<sup>-1</sup> under a compressed air purge. The results of these analyses are described in detail in an upcoming publication.<sup>27</sup>

**Nanocomposite Synthesis.** The nanocomposites were polymerized with the nanoparticles in situ. The free-radical polymerization procedure was based on the work of Balke and Hamielec.<sup>28</sup> Typically, nanoparticles (either as received (AR), coated with GPS, or dried in a vacuum (>30 in. Hg for 24 h) at 195 °C) were added to MMA monomer (15.0 g) in a 20 × 120 mm glass test tube and dispersed via sonication at 40% power (VCX-400 Sonics Materials Vibracell (400 W) with 1/4 in. stepped microtip) for 5 min. In some cases, 20  $\mu\text{L}$  of MAA was added to aid dispersion of the nanoparticles during this step (specific composite formulations are shown in Tables 2–4). The initiator (AIBN) (0.0425 g) and chain transfer agent (1-decanethiol) (30  $\mu\text{L}$ ) were added and the mixture was sonicated again for 1 additional minute. The polymerization was carried out by immersing the test tube in a 55 °C water bath under a nitrogen blanket for 21 h with two additional sonication steps of 40% power at the +1 and +2 h points. Each of these sonication steps was pulsed at 2 s ON and 0.5 s OFF with a total sonication ON time of 3 min.

Following complete polymerization, the composite was removed from the water bath and placed in a 115 °C oven for 2 h. The resulting nanocomposite was compression molded into tensile specimens (ASTM D638–95 Type IV) in a hydraulic press (Carver 12 ton) at 180 °C and 2.5 metric tons. Specimens were allowed to cool gradually to room temperature under pressure for a period of 6 h and, after removal, were sanded (400 grit) to remove flashing.

**Nanocomposite Thermal Analysis.** The glass transition temperature,  $T_g$ , was obtained through differential scanning calorimetry (DSC) (Seiko Instruments SSC5200 or Mettler Toledo DSC 822e.) Data were collected over two temperature runs from 25 to 180 °C at 10 °C min<sup>-1</sup>. Only data from the second run were used in  $T_g$  analysis, as is the standard methodology.

**Composite Mechanical Testing.** Uniaxial tension testing was performed in accordance with ASTM D638–95 at constant displacement rate of 1 mm min<sup>-1</sup> (0.04 min<sup>-1</sup> strain rate) at room temperature (nominally 25 °C) on an Instron loadframe with a 5 kN load cell and Instron extensometer ( $\pm 0.2$  in. extension). At least six samples of each material were tested, except for the neat PMMA with added MAA and the elevated temperature tests (45 °C) (Table 2) where only three samples

were tested. The extensometer had a  $\pm 20\%$  strain limit with 1 in. gage length and had to be removed for some of the tensile tests due to the extensive elongation. In these cases, sample elongation was monitored by the subsequent crosshead extension. The 1% secant modulus was determined according to the procedure of ASTM D638–95.

**Electron Microscopy.** Tensile specimen fracture surfaces were observed using a JEOL JSM-6330F field emission scanning electron microscope (SEM) after coating the polymer with gold or platinum. TEM specimens were prepared using a Leica ultracut microtome. Multiple 100 nm thick sections were cut and floated onto a #200 copper grid. In the case of necked specimens, care was taken to ensure that the diamond knife of the ultramicrotome induced no artifacts in the samples by orienting the specimen in the microtome at right angles to the tensile direction. TEM images were obtained on a JEOL CM-12.

**Polymer Physical Characterization.** Molecular weight analysis of the PMMA and nanocomposites was performed on a Waters HPLC calibrated with a narrow polystyrene standard. For the nanocomposite samples, the composite was dissolved in a solvent and the nanoparticles were centrifuged until the solution was clear before analysis by HPLC. The 17 nm composites could not be centrifuged clear due to the small size of the particles and thus were not tested. The results for number-average molecular weight ( $M_n$ ) and polydispersity index (PDI) ( $M_w/M_n$ ) for samples analyzed are shown in Table 1.

Thus, we conclude that the addition of the nanoparticles had little effect on the free-radical polymerization of the methyl methacrylate. The retained monomer concentration for neat and alumina filled PMMA samples was determined previously<sup>23</sup> with liquid <sup>1</sup>H NMR (Varian 500 MHz) and was less than 1% for all compositions. This analysis was not repeated for the samples in this report.

**Small-Angle X-ray Scattering (SAXS) Theory and Experiments.** The ability to disperse the nanoparticles in the matrix is critical to achieving the goals and expectations of nanocomposite performance and was characterized by both TEM and SAXS. X-ray scattering can be used to study structures on the order of 1 nm or larger.<sup>29</sup> As with other scattering studies of this nature,<sup>30,31</sup> the large range of nanoparticle and other feature sizes required the scattering to be performed at several facilities to capture the entire breadth of length scales. Small-angle X-ray scattering (SAXS) was performed at the National Synchrotron Light Source (NSLS), Brookhaven National Laboratory. The work was performed on beamline  $\times 10\text{A}$  with an accessible  $q$  range from 0.009 to 0.14  $\text{\AA}^{-1}$ , corresponding to real correlation lengths,  $d (=2\pi/q)$ , up to  $\sim 700\ \text{\AA}$ . The SAXS data were calibrated using the scattering from a silver behenate sample.<sup>32</sup> All scattering measurements were performed on plaques with a thickness of about 1 mm. The scattering data were normalized for thickness differences and direct beam intensity. Dark current and air background were also factored out of each data set. Ultra-small-angle X-ray scattering (USAXS) measurements were performed at the Advanced Photon Source (APS) (33-ID-D, UNICAT) located at Argonne National Laboratory. The USAXS setup utilizes a Bonse-Hart camera,<sup>33</sup> which provides “slit-smear” data in a  $q$  range of  $10^{-4}$  to  $10^{-1}\ \text{\AA}^{-1}$ . This corresponds to real correlation lengths up to 6  $\mu\text{m}$ . The data are corrected for sample thickness prior to applying a desmearing routine. To further study the anisotropy in the scattering patterns for the necked specimens, effective-pinhole collimated USAXS (SBUSAXS)<sup>34</sup> was also performed at APS. This setup does not require desmearing of the resulting data and is thus preferred for anisotropic scattering analysis.

## Results

**Nanocomposite Dispersion.** The key to accessing the large surface area-to-volume ratio of nanofillers is to optimize their dispersion within the polymer matrix. Thin specimen TEM is the method most often employed to assess the dispersion state, but it has several



**Table 2. Mechanical Properties of Neat PMMA (MAA = Methacrylic Acid)**

	1% secant modulus (GPa)	no. of tensile specimens tested	percentage of samples exhibiting yield phenomenon	av strain-to-failure (% strain)	av ultimate strength (MPa)
neat PMMA	3.0	17	12	4.5	75
neat PMMA @ 45 °C	2.6	3	0	4.5	56
neat PMMA (MAA)	2.9	3	33	8	74
2 wt % $\mu\text{m-Al}_2\text{O}_3$	3.1	5	20	5	68

**Table 3. Mechanical Properties of 38 nm Alumina/PMMA Composites<sup>a</sup>**

	1% secant modulus (GPa)	no. of tensile specimens tested	percentage of samples exhibiting yield phenomenon	av strain-to-failure (% strain)	av ultimate strength (MPa)
1.0 wt % 38 nm AR	2.7	8	50	6	62
2.2 wt % 38 nm AR	2.6	10	25	8	60
5.0 wt % 38 nm AR	2.6	6	0	5	64
1.0 wt % 38 nm (MAA)	2.4	8	75	32	56
2.2 wt % 38 nm (MAA)	2.3	10	70	40	52
5.0 wt % 38 nm (MAA)	2.5	6	25	9	56
1.0 wt % 38 nm (GPS)	3.1	6	0	4	60
2.2 wt % 38 nm (GPS)	3.1	8	0	5	70
2.2 wt % 38 nm (195)	2.5	10	60	22	57
5.0 wt % 38 nm (195)	2.8	6	0	3	58

<sup>a</sup> AR = as-received, MAA = methacrylic acid, GPS = 3-glycidoxypolytrimethoxysilane, 195 = particles dried at 195 °C in a vacuum.

**Table 4. Mechanical Properties of 17 nm Alumina/PMMA Composites<sup>a</sup>**

	1% secant modulus (GPa)	no. of tensile specimens tested	percentage of samples exhibiting yield phenomenon	av strain-to-failure (% strain)	av ultimate strength (MPa)
0.5 wt % 17 nm (MAA)	2.8	6	0	4	61
1.0 wt % 17 nm (MAA)	2.9	8	25	6	67
2.2 wt % 17 nm (MAA)	2.6	8	75	7	64
0.5 wt % 17 nm (195)	2.7	6	0	4	58
1.0 wt % 17 nm (195)	2.6	8	75	7	61
2.2 wt % 17 nm (195)	2.5	8	75	8	61

<sup>a</sup> MAA = methacrylic acid, 195 = particles dried at 195 °C in a vacuum.

drawbacks. The most obvious are the limited counting statistics and sampling frequency. SAXS, however, is well suited for determining the state of nanoparticle aggregation contained within the nanocomposites. Both SAXS and TEM were utilized in this research with similar results. Parts a–c of Figure 2 show TEM micrographs of the dispersion obtained through the above polymerization procedure with various nanoparticles. The dispersion of a 2.2 wt % 38 nm alumina nanocomposite with added methacrylic acid (MAA) dispersant is presented in Figure 2a. This image shows many isolated particles or, at worst, isolated aggregates of small particles. Figure 2b, however, shows the poor dispersion obtained with the same particles and weight fraction where no MAA was added. In this micrograph, aggregates approaching 1  $\mu\text{m}$  in size are seen with few isolated single particles. Optimal dispersion of the 17 nm particles was never achieved, as shown in Figure 2c. These finer powders are seen to agglomerate in clumps numbering hundreds of particles as opposed to the 38 nm aggregates where particles number less than 10 in most cases. Neither drying the 17 nm particles (at 195 °C and >30 in. Hg vacuum), nor adding methacrylic acid (MAA) did anything to aid in the dispersion of these smaller particles.

The dispersion conditions shown in the TEM micrographs are mirrored in the USAXS results. Parts a and b of Figure 3 show the scattered intensity ( $I(q)$ ) vs wavevector ( $q$ ) data collected on the USAXS instrument for 38 and 17 nm alumina, respectively, dispersed in PMMA at various weight fractions. Because of the large polydispersity of the alumina and the aggregation of particles, as seen in the TEM and Figure 1, standard

spherical scattering analysis cannot be carried out and only the general shape of the curves will be analyzed here. Figure 3a shows evidence that the 38 nm nanoparticles require the use of MAA to obtain better dispersion, as also noted in the TEM analysis. The topmost curve shows a large negative slope at the lowest  $q$ -vectors indicating the ever-increasing size of aggregates in composite formulations with 38 nm particles and no dispersant (MAA). However, the two lower curves show a definite decrease in slope at lower  $q$  values indicating well-dispersed, similar-size aggregates when the MAA is used in the polymerization process. This analysis confirms that the TEM micrographs of Figure 2, parts a and b, are representative of the state of dispersion in these samples.

The scattering curves obtained from various alumina/PMMA compositions with 17 nm nanoparticles are shown in Figure 3b. In these cases, even at the lowest  $q$  values the curves never approach a zero slope. Note that the curves also scale with weight fraction for all volume fractions. In fact, the curves show three distinct regions where power-law (constant slope) behavior prevails. The slope at high  $q$  values in these composites is  $-3.6$ , a value considerably greater than  $-4$ , indicating rough interfacial characteristics and quite possibly a porous-type open cell structure in the 6–15 nm regime.<sup>35</sup> In the mid- $q$  region ( $\sim 0.0017$ – $0.032 \text{ \AA}^{-1}$ ) a slope of  $-2.8$  dominates, while in the smallest  $q$  range, a slope of  $-1.1$  is seen. This type of behavior, successive power law scaling present at all length scales, is indicative of mass fractal-type aggregation where the dimensionality of the "level" is represented by the power law exponent.<sup>36</sup> The TEM image of Figure 2c is representative

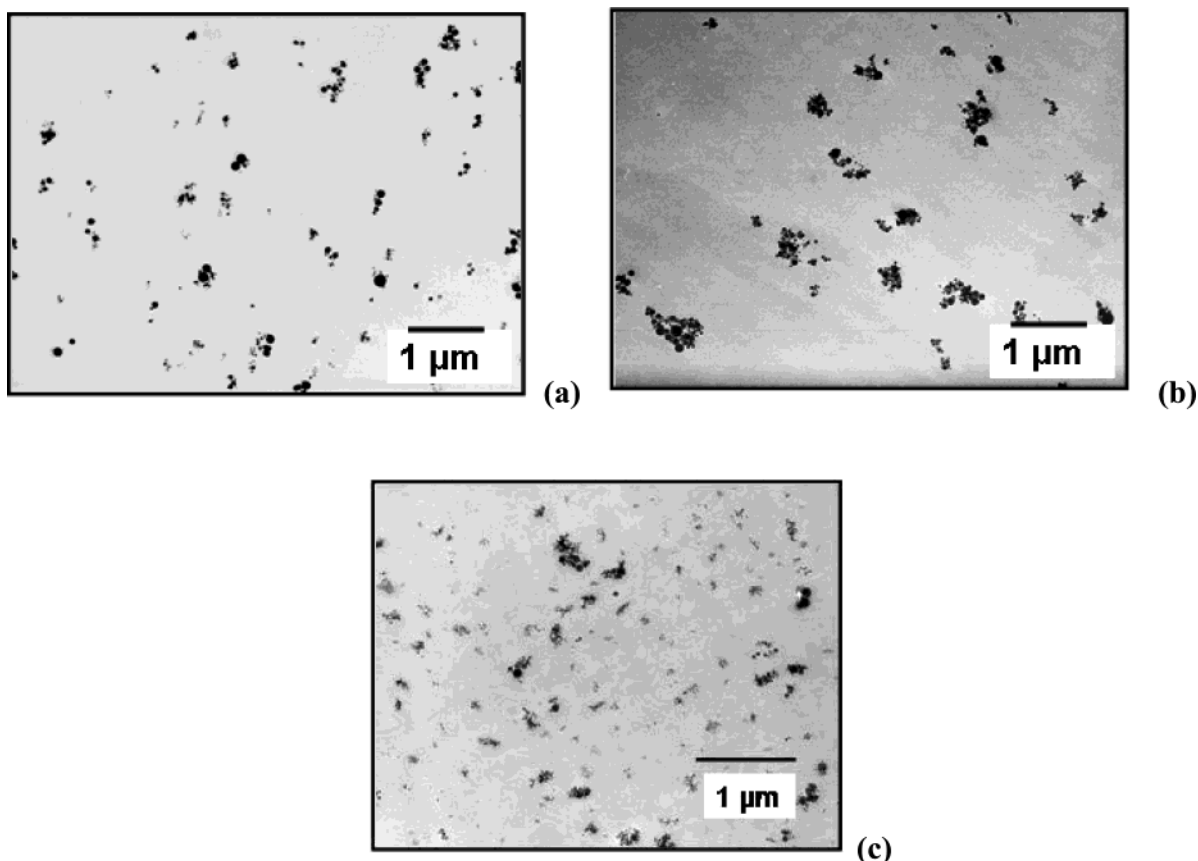


**Figure 2.** (a) 2.2 wt % 38 nm nanoparticles in PMMA with dispersant (MAA) (b) 2.2 wt % 38 nm nanoparticles in PMMA with no dispersant. (c) 2.2 wt % 17 nm nanoparticles in PMMA (shown here with added MAA dispersant).

of the fractal nature of the nanofillers in these composites. Fractal aggregates can be well-dispersed in a polymer matrix, but the goal of individually occurring, well-dispersed single particles or aggregates was never realized in these 17 nm composites.

**Thermal Behavior.** The glass transition temperature,  $T_g$ , of the alumina/PMMA nanocomposites exhibits a sharp decrease from 119 °C for the neat PMMA to 95 °C following the addition of a small volume fraction of as-received nanoparticles<sup>24</sup> (0.5 wt % 17 nm alumina or 1.0 wt % 38 nm alumina) as shown in Figure 4. This lower value of  $T_g$  (95 °C) is maintained for filler weight fractions up to 5 wt %. For composites with less than a critical weight fraction of 38 nm nanoparticles, the  $T_g$  is constant, within experimental error, at the  $T_g$  of the neat PMMA used in this study. The  $T_g$  of the neat PMMA is regained for composites synthesized with GPS-modified nanoparticles (Figure 4) as well as those made with as-received micrometer-sized alumina (not shown). In addition, other work by these authors has shown that the  $T_g$  of the neat polymer remaining when the nanoparticles are removed returns to 119 °C.<sup>24</sup> The thermal behavior is thus highly interface dependent in addition to being sensitive to the size of the particles and is discussed in detail in an upcoming publication.<sup>27</sup>

**Mechanical Behavior.** The most striking behavior displayed by these nanocomposites is seen in the stress-strain curves presented in Figure 5. In this graph, a typically brittle PMMA is compared with a 2.2 wt % (0.73 vol %) 38 nm (with MAA dispersant) alumina/PMMA nanocomposite that displays ductile behavior at a strain rate of 4% strain  $\text{min}^{-1}$ . Typically, in samples where the nanoparticle loading is optimized, this remarkable transition from brittle to ductile behavior is

observed with the average strain-to-failure increasing to 40%. These large extensions were observed in 70% of the samples tested. In nanocomposites that do not show ductile behavior, preexisting flaws or inclusions (from the breaking, molding, and finishing process) were often observed that initiated sample failure.

In addition to the dramatic increases in the strain-to-failure, a drop in the modulus was observed and a neck occurred coincident with a drop in engineering stress in the region past a well-defined yield point. It is also noted that the yield strength of the nanocomposite lies some 20 MPa below that of the neat PMMA, which typically failed in a brittle fashion at 4% strain. The micrometer-sized filled composite, at 2 wt %, shows brittle behavior much like that of the neat PMMA.

In an effort to make the surfaces of the particles more compatible with the matrix, 38 nm alumina nanoparticles were coated with a silane coupling agent (3-glycidypropyltrimethoxysilane (GPS)). Nanocomposites made from these coated particles did, in fact, have a modulus slightly above that of the neat PMMA and their yield strength was increased to 70 MPa, roughly that of neat PMMA. However, these composites also reverted back to the same brittle behavior as shown in Figure 6.

Samples of neat PMMA were also tested at temperatures above room temperature (i.e., at 45 °C) to determine whether a temperature increase of 20 °C could induce the change from brittle to ductile behavior.<sup>23</sup> This temperature increase was chosen to mimic the reduction in glass transition temperature typically shown by the nanocomposites, as mentioned above. Neat PMMA has been shown to yield in a manner similar to the nanocomposites at elevated temperatures and much

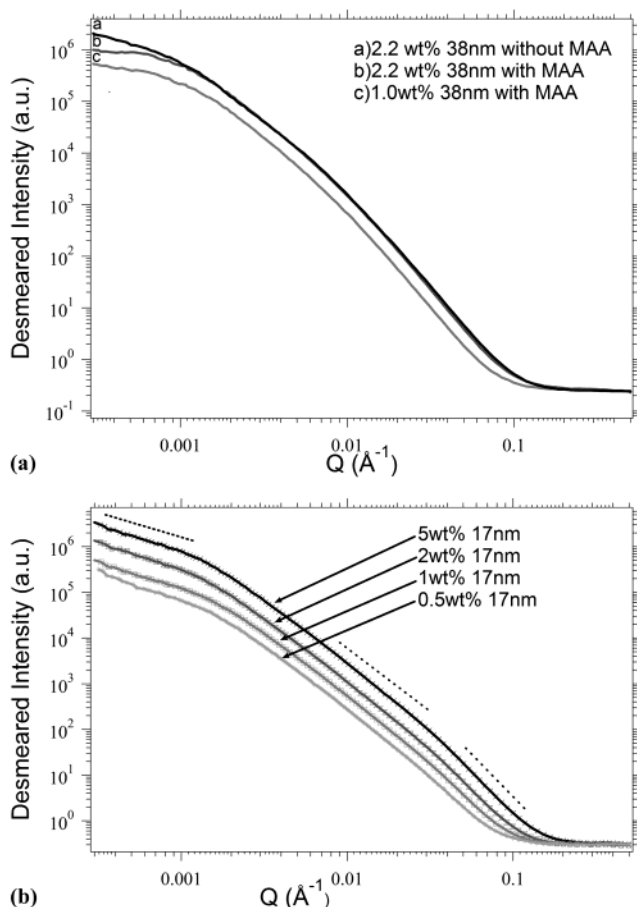


**Figure 3.** USAXS data for (a) 38 nm alumina nanocomposites and (b) 17 nm alumina (with MAA dispersant) nanocomposites.

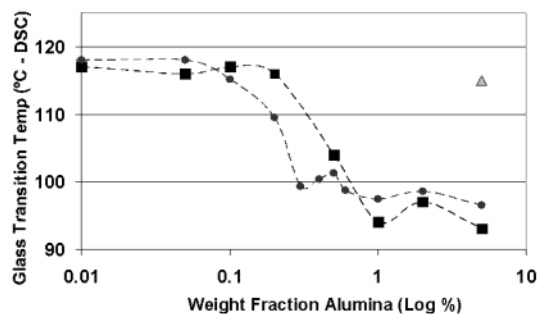


**Figure 4.** Glass transition behavior of as-received alumina/PMMA nanocomposites ( $\square$ , 38 nm alumina;  $\circ$ , 17 nm alumina). Note that the filler weight fraction is plotted on a log scale to show the behavior of the lower values more clearly. The neat PMMA is plotted as 0.01 wt % on the above graph. Following coating with GPS, the  $T_g$  returns to the neat value ( $\blacktriangle$ , GPS-coated).

lower strain rates.<sup>37</sup> In these elevated temperature runs, the initial modulus matches that of the filled system, but the yield strength drops even lower than that of the 2.2 wt % (0.73 vol %) 38 nm alumina/PMMA nanocomposite samples tested at room temperature. In addition, the strain-to-failure shows no increase, with the sample still failing at the yield point ( $\sim 4\%$  strain). The neat PMMA had to be tested at 80 °C for ductile behavior to be realized.

Of the various 17 nm nanocomposites tested, none showed the large increases in strain-to-failure, with all samples failing at or just slightly past the yield point. As noted before, however, these composites did display

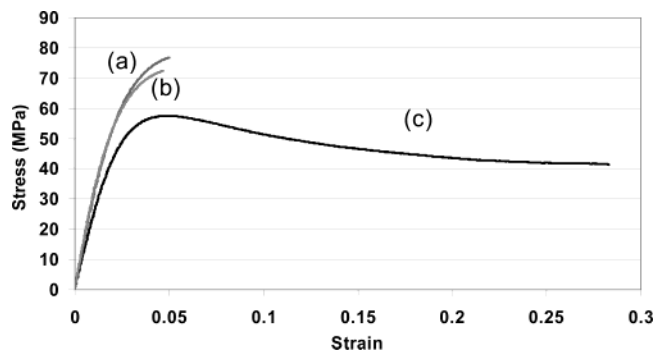


**Figure 5.** Typical stress-strain curves for (a) neat PMMA, (b) 2 wt % as-received micrometer-sized alumina filled/PMMA composite, and (c) 2.2 wt % 38 nm (MAA) alumina/PMMA nanocomposite. The crosshead speed was 1 mm/min, which translates to a 0.04  $\text{min}^{-1}$  rate.

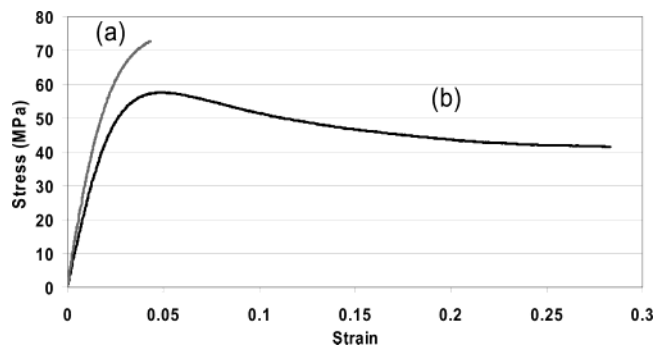


**Figure 6.** Stress-strain curves for (a) 2.2 wt % GPS-coated 38 nm alumina/PMMA nanocomposite compared to (b) the ductile 2.2 wt % 38 nm (MAA) alumina/PMMA nanocomposite. The crosshead speed was 1 mm/min, which translates to a 0.04  $\text{min}^{-1}$  rate.

the same glass transition behavior as 38 nm compositions exceeding 0.5 wt % nanoparticles.

Tables 2–4 provide a summary of the mechanical data for the various composite and neat formulations used in this study. In Table 3, a maximum in the strain-to-failure behavior is seen for 38 nm nanoparticles at 2.2 wt % (0.73 vol %), with the majority of these specimens (70%) failing in a ductile fashion (average strain-to-failure 40%). It is noted, however, that the 1.0 wt % samples also showed a high fraction of ductile failures, although the average strain-to-failure for this composition was lower. This was similar to the results in our previous work where the maximum for 39 nm alumina nanoparticles in PMMA (a different lot of alumina nanoparticles from Nanophase Technologies) occurred at 5 wt %.<sup>23</sup> The observation of a particular weight fraction at which mechanical behavior is optimized has been observed in other nanocomposite studies.<sup>4,13,38,39</sup> It is obvious that at lower particle loadings, there is generally not enough material altered by the presence of the particles to permit large-scale changes in material properties. Higher loadings induce agglomeration, which degrades the polymer performance through, for example, inclusion of voids that can act as preferential sites for crack initiation and failure. As stated in the Experimental Section, the use of a dispersant (MAA) was required to obtain the large strain-to-failures observed; 38 nm samples with no dispersant showed little to no increase in strain-to-failure (Table 3). Note also that the addition of methacrylic acid to the neat PMMA does not lower the modulus or lead to a brittle-to-ductile transition (Table 2). It is also noted



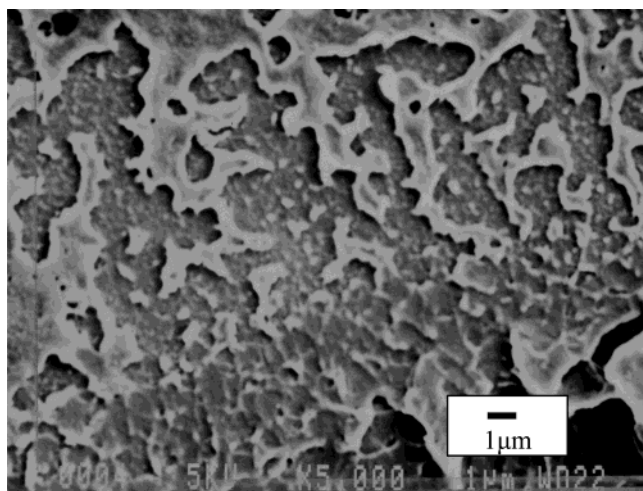


**Figure 7.** SEM image of the fracture surface of a neat PMMA specimen showing the evidence of crazing (raised hackle bands).

that drying the 38 nm nanoparticles in a vacuum oven at 195 °C overnight did induce the change from brittle to ductile behavior at one of the two weight fractions tested (2.2 wt %).

The reduction in the glass transition temperature most certainly affects the mechanical properties presented in Tables 3 and 4. Of particular note, the modulus of the nanocomposites drops from 3.0 to 2.5 GPa for most compositions. This decrease in modulus is almost certainly due to the decrease in the glass transition temperature. As shown in Table 2, for the elevated temperature experiments on neat PMMA, the modulus shows a similar drop as that displayed in the nanocomposites. In fact, all of the nanocomposites showed a perfect correspondence between their modulus decrease and the displayed reduction in their glass transition temperature. Thus, any modulus gain (or decrease) due to the addition of nanoparticles would have been overshadowed by the dependence of the modulus on the testing temperature, or, in this case, the *a priori* reduction in the glass transition temperature.

The yield stress of the nanocomposites is also shown to decrease in much the same fashion as the secant modulus. This, too, was caused by the reduction in the glass transition temperature. It is well-known that the yield stress of a polymer is directly related to the testing temperature with an increase in testing temperature causing a reduction in the modulus.<sup>40</sup> In support of this hypothesis, the yield stress and modulus of the neat PMMA in tension at an elevated temperature (simulating a  $T_g$  depression) showed a decrease (Table 2) that matched that of the nanocomposite.

**Fracture Surface Microscopy.** The fracture surface morphology of the neat polymer shown in Figure 7 is similar to those of neat PMMA fracture surfaces found in the literature. The prominent raised features, known as hackle bands, are attributed to craze formation and propagation.<sup>41</sup> Strikingly different, the fracture surface of one of the ductile composites is presented in Figure 8, parts a and b. In Figure 8a, the fracture surface is fairly flat and marked only by a uniform distribution of small holes. In this Figure, there are no attributes of craze formation or growth. In Figure 8b, nanoparticles are seen sitting in some of the voids. Other voids are not occupied by particles. In general, no connecting

polymer from void to nanoparticle can be seen. This suggests that dewetting of the particles from the matrix occurred either prior to or during mechanical testing. That the particles do not show an affinity for the polymer is not surprising considering the complicated synthesis procedure required to optimize the nanoparticle dispersion. The fracture surface of the nanocomposites shown in Figure 8b indicates that the nanoparticles appear to nucleate voids. This surface, however, was created by brittle fracture of the material following ductile yielding and therefore could be very different from the conditions existing within the bulk just before fracture. Therefore, SAXS was used to determine the composite morphology and the status of the voids that existed within the bulk immediately before fracture in the heavily necked sections of the tensile specimen and is reported in the next section.

In the SEM micrograph of Figure 8c, the particles do not appear to be interacting with the matrix in any fashion (no evidence of ductile tearing of the polymer around the particle or hemispherical cavities as seen in Figure 8b). In fact, the fracture behavior of the surface does not appear to depend on the presence or absence of the nanoparticles. These particles have been coated with a silane coupling agent (GPS) to promote matrix wetting. The surface of a 2.2 wt % (0.73 vol %) 38 nm GPS–alumina composite shows well-dispersed nanoparticles sitting on the fracture surface. The composite properties associated with these coated nanoparticle composites are given in Table 3 and amount to a restoration of the yield strength and modulus accompanied by a return to brittle behavior at room temperature.

**Small-Angle X-ray Scattering.** To determine the extent of the void creation occurring within the neck of the ductile nanocomposites, a method that samples the volume within the neck is required. Because of the contrast differences between the voids and nanoparticles, these additional scattering entities (the voids) should scatter X-rays and allow for the study of their morphology through SAXS. The first scattering experiments conducted on the necked portion of the nanocomposites were carried out at the National Synchrotron Light Source. The raw 2D scattering profile gives an initial look at the interior morphology of the strained nanocomposite. As shown in Figure 9a, the scattering from the nanocomposite outside of the neck is isotropic, centered on the black disk of the beamstop. Figure 9b shows the scattering pattern detected when the necked portion of the sample was placed in the beam. An anisotropic, ellipsoidal pattern is clearly indicated in this case with the major axis aligned parallel to the tensile direction and the scattering intensity at the poles twice that at the equator. In this case, the scattering intensity is shifted toward the higher  $q$  value regime (away from the beamstop) indicating the presence of a “new”, smaller, oriented scatterer. Since the additional intensity in the anisotropic scattering pattern is occurring at higher values of  $q$ , these new scatterers have their minor axis aligned in that (the tensile) direction, with the major axis aligned along the equator.

Crazing in polymers also produces an anisotropic scattering pattern; however, the crazing pattern can be easily identified as it appears as two perpendicular crosslike streaks.<sup>42</sup> The absence of these streaks in the sample's scattering pattern provides direct evidence that the anisotropic scattering pattern is not due to

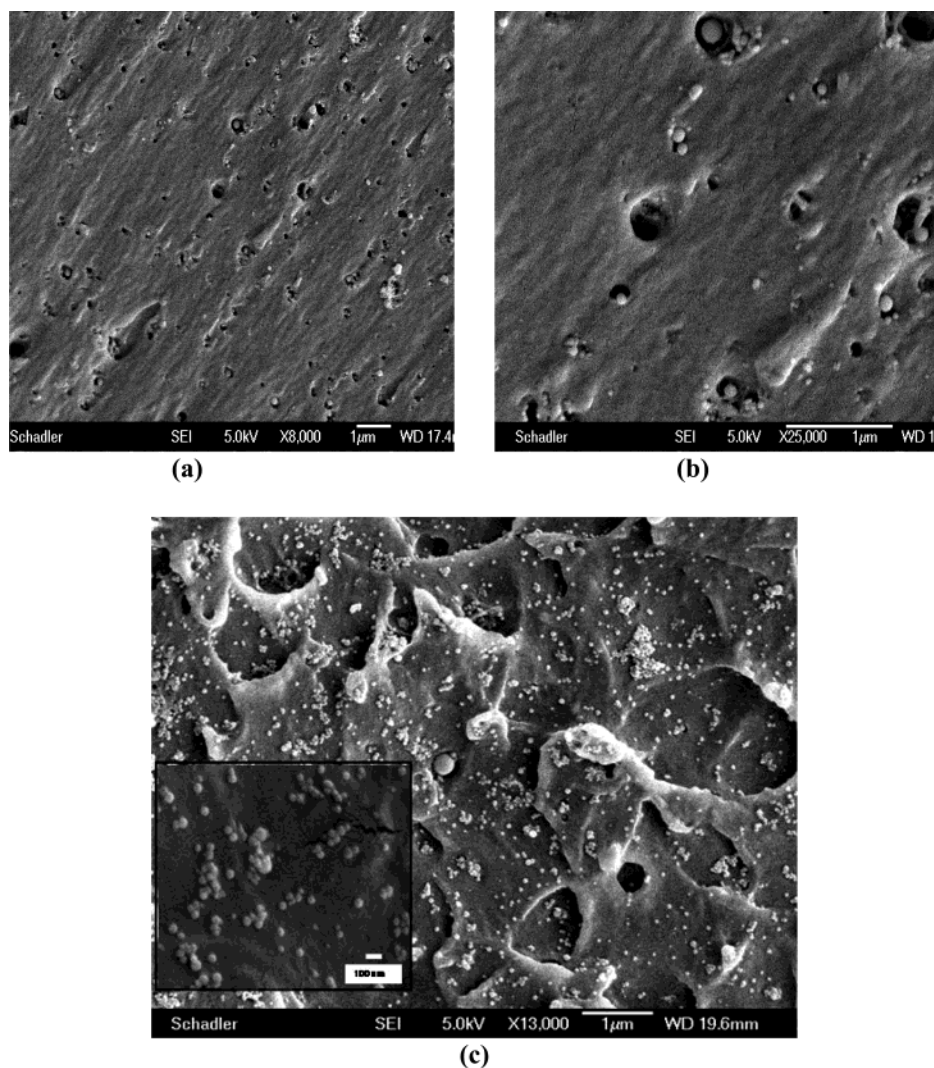


**Figure 8.** (a, b) FE-SEM images showing the fracture surface of a 2.2 wt % 38 nm (MAA) alumina/PMMA ductile tensile specimen with an ultimately brittle failure. Notice the uniform dispersion of “holes” that is seen in part a and magnified in part b. (c) FE-SEM micrograph of the fracture surface of a 2.2 wt % 38 nm GPS-coated alumina/PMMA sample. Note that the particles still show little affinity for the matrix and do not appear to be nucleation sites for the features on the fracture surfaces (inset).

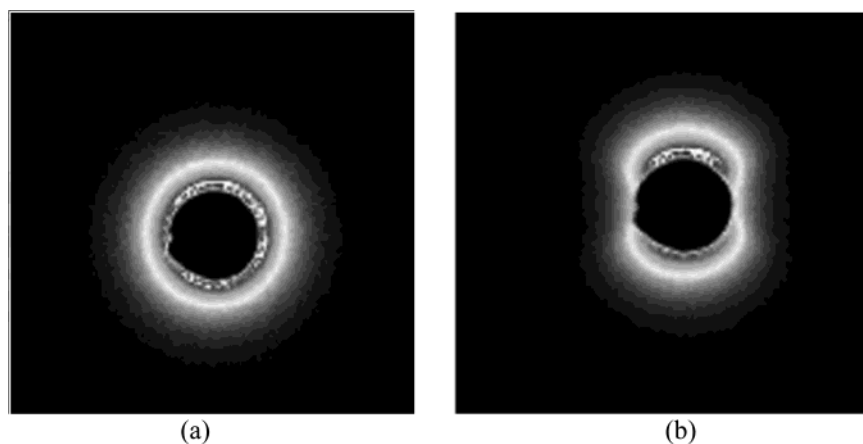


**Figure 9.** 2-D small-angle X-ray scattering intensity of a 2.2 wt % 38 nm (MAA) alumina/PMMA nanocomposite (a) out of the necked area and (b) in the necked area. The tensile direction is vertical in relation to the observed scattering pattern.

craze features within the neck. In fact, these data indicate that crazed material is not present within the neck.

Additional scattering using the single-bounce ultra-small X-ray scattering (SBUSAXS) technique (Figure 10) shows the intensity vs  $q$ -vector data obtained when

the necked specimens are oriented in different directions with respect to the X-ray beam. The curves show different scattering profiles at two different angles, clearly indicating the anisotropy shown in Figure 9b with much better resolution in the low  $q$  range. As seen in Figure 10b, the scattered intensity is much higher



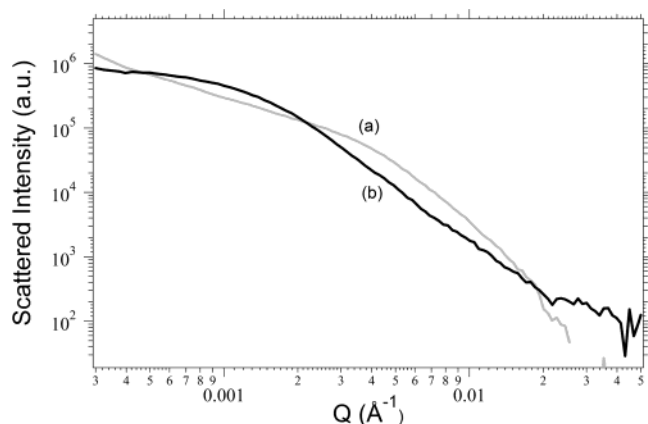


**Figure 10.**  $I(q)$  vs  $q$  (SBUSAXS) in the necked area in a 2.2 wt % 38 nm (MAA) alumina /PMMA nanocomposite. The scattering from curve a is the polar direction while curve b represents the equatorial component. Curve a shows the same anisotropic features seen in Figure 9b, namely a higher scattering intensity at  $q$  values between 0.0025 and 0.01  $\text{\AA}^{-1}$  for scattering at the poles, while curve b shows the scattered intensity typical of isotropic scatterers (as in Figure 9a).

in the direction parallel to the tensile axis than in the equatorial direction (at  $q \approx 0.005 \text{ \AA}^{-1}$ ). In addition, the curves are shown to cross over at lower  $q$ -vectors, indicating some population of larger scatterers that are also anisotropic, but have their small correlation length aligned perpendicular to the tensile direction.

With this knowledge and the available fracture surface pictures (Figure 8b), a model of the scattering entity can be suggested, as shown in the inset of Figure 11. This image shows a picture of a nanoparticle where a void has formed above and below the nanoparticle due to the action of tensile stress. The shaded ellipses, above and below the particle, represent idealized scatterers that could be used to model the scattering data presented in Figures 9b and 10. This model has been used before to explain anisotropic SAXS patterns in similar hard-filler, debonded particle composites.<sup>43</sup> To determine the nature of this anisotropic scattering entity, and to prove that voids were indeed expanding from the poles of the particles, TEM specimens of the necked region were prepared and analyzed. Careful sectioning of the specimen with the cutting direction perpendicular to the tensile direction was carried out to avoid artifacts created by the diamond knife from being misinterpreted in the TEM analysis. One of the micrographs taken in the necked region is shown in Figure 11. There are two features that are worth noting on this representative micrograph. The first is the existence of ellipsoidal voids on the poles (with respect to the tensile direction) of the larger nanoparticles. As can be corroborated from the SEM fracture surfaces (Figure 8b), however, only certain size particles initiate void creation. The second feature is the chainlike aggregates of smaller nanoparticles that appear to have aligned themselves in the direction of the applied force. These appear to be two possible anisotropic candidates for the additional scattering entity alluded to in the scattering curves presented above. However, the anisotropic scattering patterns in Figure 9b, and at the higher  $q$ -vectors in Figure 10, cannot be due to the nanoparticle chains. This is because the elongation is occurring in the direction of the tensile force and thus would tend to shift the scattering in this direction to lower  $q$  (larger size scales), not higher  $q$  as seen above. Scattering that was at-

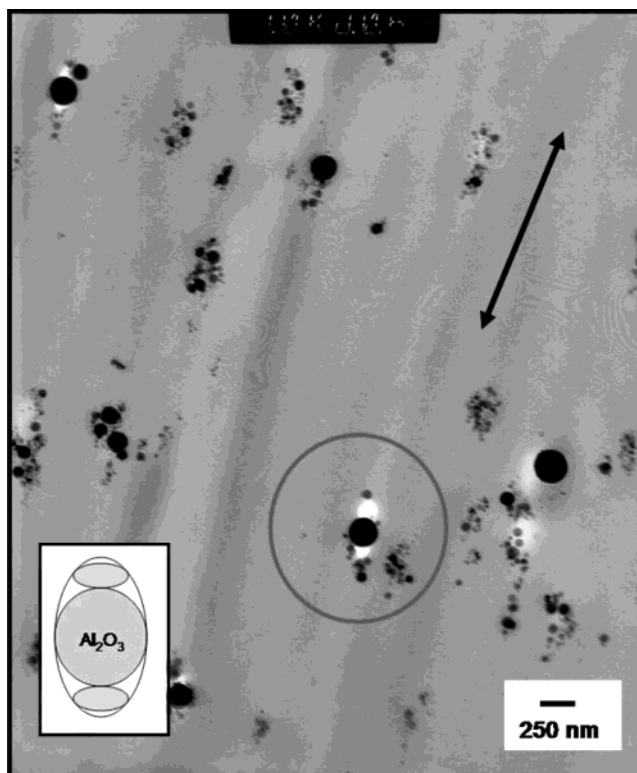


**Figure 11.** TEM micrograph of the necked area in a 2.2 wt % (0.73 vol %) 38 nm (MAA) alumina/PMMA composite with ductile behavior. Note the semi-circular voids that exist above/below two of the larger particles in the micrograph. The double-headed arrow indicates the direction of the tensile stress. Inset: Model of a single ellipsoidal void surrounding a nanoparticle and aligned in the tensile direction. The small ellipses above and below are the author's hypothesis of the scattering entities responsible for the observed scattering pattern.

tributed to these particles would have resulted in an anisotropic pattern oriented perpendicular to the tensile direction, where the smaller length scale is seen. In fact, the crossover of SBUSAXS curves shown in the lower  $q$  regions may be due to these strings of nanoparticles.

## Discussion

In a uniaxial tensile test, high molecular weight poly-(methyl methacrylate) (PMMA) typically fails in a brittle fashion at roughly 4% strain.<sup>44</sup> As shown in Figure 5, the neat PMMA polymer synthesized in this study displays this brittle behavior at the temperature and strain rate regimes tested. This familiar brittle behavior is related to normal stress yielding, a cavitation mode that involves the formation and coalescence of crazes that usually lead to cracking and eventual failure at low strains.<sup>45</sup> With the addition of a small amount of alumina nanoparticles, however, PMMA undergoes a transition from brittle-to-ductile behavior with the appearance of a well-defined yield point, pronounced necking, and a tremendous increase in strain-to-failure (Figure 5). Neat PMMA can also undergo this brittle-to-ductile transition, at low enough strain rates or high enough temperatures. In the present work, the synthesized PMMA did not exhibit ductile behavior in uniaxial tension until the temperature was raised to 80 °C, a temperature only slightly higher than other researchers have reported (65 °C).<sup>46,47</sup> On the other hand, the nanocomposite undergoes this transformation in uniaxial tension at room temperature.

The yielding phenomenon of polymers is highly time and temperature dependent with the competition between shear and dilatational yielding integrally linked to the local stress state of each volume element in the material. Therefore, a transition from brittle-to-ductile behavior can occur if the stress state in the polymer is changed in such a way that the shear yield criterion is reached prior to the formation of crazes (i.e., homogeneous yielding by shear vs heterogeneous yielding by crazing).<sup>48</sup> Ductility is thus gained by the delocalization of yielded material and suppression of crazes that could lead to void formation and subsequent brittle behavior. This type of phenomenon has been extensively reported in rubber filled epoxies.<sup>8,9,15,49</sup> In these cases, the researchers noticed the same features as can be seen in Figure 8b, that is, the apparent dewetting of the rubber particle within the matrix. Unlike the oxide particles used in this study, however, rubber particles also cavitate, creating voids interior to the particles, during mechanical testing. This cavitation, also seen in rubber-filled nylon-6,<sup>12</sup> is hypothesized to bring about localized shear yielding in the vicinity of the particles by relieving the triaxial stress-state that prevents incipient void formation in the matrix. Thus, the sequence of cavitation, stress-state transition from plane strain to plane stress, ligament yielding, and propagation of yielded areas through connectivity of the ligaments would lead to a tougher matrix, especially if the yielding was greatly delocalized and affected a large volume fraction of the matrix polymer.<sup>12</sup> Well-dispersed nanoparticles acting as void nucleation sites would also ensure that the regions of stress-state transformation occur throughout the composite, delocalizing the damage and maintaining the stability of the deformation process.

The behavior of a ductile material containing a volume fraction of voids has been analyzed by Gurson<sup>50</sup> and applied to rubber-toughened polymers by Lazzeri and Bucknall.<sup>8</sup> Their analysis concluded that yielding occurred in these materials through the formation of dilatation bands, which allow the original voids to expand as plastic flow occurs in the intervening ligaments. Therefore, precraze void formation leading to crazing is prevented, and shear yielding of the matrix is favored as the primary yield mechanism. However, the brittle-to-ductile behavior is not seen at all filler volume fractions, as indicated in Table 3 and previous research,<sup>23</sup> because agglomerates of the nanoparticles act as crack initiators that lead to premature brittle failure. On the other hand, lower particle loading does not affect enough of the matrix to delocalize the damage and prevent the formation of stable crazes. Thus, there is an optimum range of filler that promotes this brittle-to ductile behavior.

As observed in the TEM micrograph of Figure 11, and in the SEM micrographs of Figure 8b, the smaller particles do not appear to take part in the creation of polar voids. Thus, it would appear that only larger particles, those on the order of 100–200 nm in diameter, are responsible for the void growth, subsequent strain-state transformation, and ultimate brittle-to-ductile transformation. This is not surprising given the size of the smaller particles and the ability of a void to grow around them. Gent and Tomkins<sup>51</sup> have shown that the triaxial stress required to grow an incipient void varies inversely with the void's initial radius. The authors point to the absence of voids around particles of carbon-

black, which are normally 5–20 nm in size, in filled elastomers as proof of the relevance of initial particle size to void formation and growth. In addition, Lazzeri and Bucknall use an energy criterion to predict the optimum size of rubber particles that will cavitate in brittle PS polymer.<sup>52</sup> Their predictions show that void creation (and strain relief) occur in the largest particles first and then move to smaller particles in accordance with the ease of void nucleation.

In the present work, the presence of larger, non-interacting nanoparticles alone (and the subsequent void expansion), does not lead to the brittle-to-ductile behavior as shown in Table 3. Following coating the nanoparticles with GPS, the data show that the yield strength and modulus of the nanocomposite match the respective properties of neat PMMA, accompanied by a subsequent loss of the brittle-to-ductile behavior. These particles have the same size distribution before coating as after, and the dispersion in the matrix is similar, as shown by the SEM micrograph of Figure 8c. These nanocomposites also do not show a reduction in the glass transition temperature, indicating no increase in polymer chain mobility due to the large surface area of the included nanoparticles. It is clear from these data that the surface of the coated nanoparticles has been made somewhat more compatible with the PMMA matrix. However, it would seem that the ability of the polymer to wet the particles has not drastically changed, as shown in the SEM micrograph of Figure 8c. In this micrograph, the particles are seen to sit on the fracture surface, showing no signs of wetting or participation in the fracture morphology. In recent modeling experiments, van Melick et al.<sup>53</sup> found that, in addition to voids introduced into polystyrene, extra chain mobility due to the surface area contained in the voided system was required for a brittle-to-ductile transition. This extra mobility is certainly absent in the GPS-coated alumina nanocomposites as evidenced by the stable  $T_g$ . Therefore, even with the large particles present with relatively poor wetting characteristics, the brittle-to-ductile transition phenomenon requires further input.

The role of mobility in the yielding behavior of polymers was thoroughly examined by Wu<sup>54</sup> who related the characteristic ratio,  $C_\infty$ , and the entanglement molecular weight,  $M_E$ , to arrive at a molecular criterion for determining whether a polymer would craze or yield. He determined that a polymer having a small  $M_E$  or large  $C_\infty$  will tend to craze instead of yield due to the low ratio of crazing to yield stress. In a recent series of papers, Yee et al. also explored the role of molecular mobility in the transition from brittle to ductile behavior by altering the backbone of pseudo-polycarbonate polymers with the incorporation of other, mobile or sessile monomers into the polymer chain.<sup>55–57</sup> They concluded that the increased mobility of the backbone brought about a drop in the overall yield stress so that it remains below the brittle, crazing stress criterion. Thus, enhanced mobility can change the yielding mode of a polymer by shifting the crazing stress higher while shrinking the shear yielding surface, thus ensuring that the shear yield criterion is reached before the craze criterion in uniaxial tension.

The mobility of the synthesized nanocomposites has indeed increased as observed indirectly through the reductions in the glass transition temperature and directly in past solid-state NMR experiments.<sup>23</sup> However, the brittle-to-ductile transition was not achieved

in the 17 nm alumina filled samples (Table 4). In addition, the neat PMMA does not display a shift from crazing to shear yield until tested at temperatures far above 45 °C (room temperature + 20 °C). This calls into question the use of the mobility argument of Yee et al. as it would apply to the present work. However, the extra mobility would lower the shear yield stress and also increase the probability of nucleating stable crazes within the nanocomposites.

Thus, the complete story alumina/PMMA nanocomposite ductility requires both effects, the higher mobility of the polymer brought about by the added surface area (and evidenced by the decrease in observed  $T_g$ ), and the existence of larger particles to allow void growth and subsequent relief of the triaxial stress state (as shown in the SEM, SAXS and TEM data). This allows the strain state to be reduced to a plain stress condition, which leads to subsequent shear yielding. Because the triaxial stress is relieved, normal yielding by cavitation and subsequent crazing is prohibited and the material shows a ductile response to tensile loading.

## Conclusions

Polymer nanocomposites were synthesized while varying the filler particle size and interfacial character. When a weak interface exists between nanoparticle and polymer the room temperature mode of yielding was changed from normal (cavitation) to shear, which led to a brittle-to-ductile transition. This phenomenon was shown to require both the enhanced polymer chain mobility attributed to smaller particles and the ability to relieve the stress triaxiality by poorly bonded larger particles. It should not be limited to alumina/PMMA nanocomposites, but should be applicable to any glassy, amorphous thermoplastic with nanoscale inclusions that are poorly bonded to the matrix polymer.

**Acknowledgment.** This work was supported by the Nanoscale Science and Engineering Initiative of the National Science Foundation under NSF award numbers DMR-0117792 and CTS-9871894 and by the Office of Naval Research under grant number N00014-99-1-0187. The authors would like to thank S. S. Sternstein, B. C. Benicewicz, A. Eitan, and J. Tkacik of RPI for many thoughtful hours of discussion. In addition, we thank Y. A. Akpalu (RPI) and P. Thiyagarajan (Intense Pulsed Neutron Source, ANL) for devoting considerable time in discussing the theory, execution, and analysis of the X-ray scattering contained in this work. The TEM specimens were prepared at the Cornell Integrated Microscopy Center, Cornell University, with the help of Dr. Yuanming Zang. We would also like to acknowledge the Mettler-Toledo Thermal Analysis Educational Grant for donation of the DSC instrument to the RPI New York State Center for Polymer Synthesis. Ultra-small-angle X-ray scattering (USAXS) performed at the UNICAT facility (33-ID-D) at the Advanced Photon Source (APS) (Argonne National Laboratory, Argonne, IL) is supported by the University of Illinois at Urbana-Champaign, Materials Research Laboratory (U.S. Department of Energy (DOE), the State of Illinois-IBHE-HECA, and the NSF), the Oak Ridge National Laboratory (U.S. DOE under contract with UT-Battelle LLC), the National Institute of Standards and Technology (U.S. Department of Commerce), and UOP LLC. The APS is supported by the U.S. Department of Energy, Basic Energy Sciences, Office of Science, under Contract

No. W-31-109-ENG-38. Beamline X10A (SAXS) is supported by Exxon Mobil Research and Engineering Co. at the National Synchrotron Light Source, Brookhaven National Laboratory, which is supported by the U.S. Department of Energy, Division of Materials Sciences and Division of Chemical Sciences, under Contract No. DE-AC02-98CH10886. Sandia is a multiprogram laboratory operated by the Sandia Corporation, a Lockheed Martin Company, for the United States Department of Energy's National Nuclear Security Administration under Contract DE-AC04-94AL85000.

## References and Notes

- (1) Sumita, M.; Tsukumo, Y.; Miyasaka, K.; Ishikawa, K. *J. Mater. Sci.* **1983**, *18*, 1758.
- (2) Hussain, M.; Nakahara, A.; Nishijima, S.; Niihara, K. *Mater. Lett.* **1996**, *27*, 21.
- (3) Sumita, M.; Tsukumi, H.; Miyasaka, K.; Ishikawa, K. *J. Appl. Polym. Sci.* **1984**, *29*, 1523.
- (4) Ou, Y.; Yang, F.; Yu, Z. *J. Polym. Sci., Part B: Polym. Phys.* **1998**, *36*, 789.
- (5) Petrovic, Z. S.; Zhang, W. *Mater. Sci. Forum* **2000**, *352*, 171.
- (6) Ji, X. L.; Jing, J. K.; Jiang, W.; Jiang, B. Z. *Polym. Eng. Sci.* **2002**, *42*, 983.
- (7) Takayangi, M.; Vemura, S.; Minami, S. *J. Polym. Sci., Part C* **1964**, *5*, 113.
- (8) Lazzeri, A.; Bucknall, C. B. *J. Mater. Sci.* **1993**, *28*, 6799.
- (9) Bucknall, C. B. In *Polymer Blends, Volume 2: Performance*; Paul, D. R., Bucknall, C. B., Eds.; John Wiley & Sons: New York, 2000; Chapter 22.
- (10) Gilbert, D. G.; Donald, A. M. *J. Mater. Sci.* **1986**, *21*, 1819.
- (11) Jansen, B. J. P.; Rastogi, S.; Meijer, H. E. H.; Lemstra, P. J. *Macromolecules* **2001**, *34*, 3998.
- (12) Wu, S. *J. Appl. Polym. Sci.* **1988**, *35*, 549.
- (13) Becker, C.; Krug, H.; Schmidt, H. *Mater. Res. Soc. Symp. Proc.* **1996**, *435*, 237.
- (14) Wu, S. *Polymer* **1985**, *26*, 1855.
- (15) Pearson, R.; Yee, A. *J. Mater. Sci.* **1991**, *26*, 3828.
- (16) Abboud, M.; Turner, M.; Duguet, E.; Fontanille, M. *J. Mater. Chem.* **1997**, *7*, 1527.
- (17) Wang, S.; Wang, M.; Lei, Y.; Zhang, L. *J. Mater. Sci. Lett.* **1999**, *18*, 2009.
- (18) Caris, C.; van Elven, L.; van Herk, A.; German, A. *Br. Polym. J.* **1989**, *21*, 133.
- (19) Rong, M. Z.; Zhang, M. Q.; Zheng, Y. X.; Zeng, H. M.; Friderich, K. *Polymer* **2001**, *42*, 3301.
- (20) von Werne, T.; Patten, T. *J. Am. Chem. Soc.* **2001**, *123*, 7497.
- (21) Weimer, M. W.; Chen, H.; Giannelis E. P.; Sogah, D. Y. *J. Am. Chem. Soc.* **1999**, *121*, 1615.
- (22) Tsubokawa, N.; Kogure, A.; Maruyama, K.; Sone, Y.; Shimomura, M. *Polym. J.* **1990**, *22*, 827.
- (23) Ash, B. J.; Rogers, D. F.; Wiegand, C. J.; Schadler, L. S.; Siegel, R. W.; Benicewicz, B. C.; Apple, T. *Polym. Compos.* **2002**, *23*, 1014.
- (24) Ash, B. J.; Schadler, L. S.; Siegel, R. W. *Mater. Lett.* **2002**, *55*, 83.
- (25) Tsubokawa, T.; Kogure, A.; Maruyama, K.; Sone, Y.; Shimomura, M. *Polym. J.* **1990**, *22*, 827.
- (26) Abboud, M.; Turner, M.; Duguet, E.; Fontanille, M. *J. Mater. Chem.* **1997**, *7*, 1527.
- (27) Ash, B. J.; Siegel, R. W.; Schadler, L. S. Submitted for publication in *J. Polym. Sci., Part B: Polym. Phys.* **2003**.
- (28) Balke, S. T.; Hamielec, A. E. *J. Appl. Polym. Sci.* **1973**, *17*, 905.
- (29) Roe, R. J. *Methods of X-ray and Neutron Scattering in Polymer Science*; Oxford University Press: New York, 2000; p 155.
- (30) Beaucage, G.; Rane, S.; Schaeffer, D. W.; Long, G.; Fischer, D. *J. Polym. Sci., Part B: Polym. Phys.* **1999**, *37*, 1105.
- (31) Skillas, G.; Agashe, N.; Kohls, D. J.; Ilavsky, J.; Jemian, P.; Clapp, L.; Schwartz, R. J.; Beaucage, G. *J. Appl. Phys.* **2002**, *91*, 6120.
- (32) Huang, T. C.; Toraya, H.; Blanton, T. N.; Wu, Y. *J. Appl. Crystallogr.* **1993**, *26*, 180.
- (33) Bonse, U.; Hart, M. *Appl. Phys. Lett.* **1965**, *7*, 238.
- (34) Ilavsky, J.; Allen, A. J.; Long, G. G.; Jemian, P. R. *Rev. Sci. Instrum.* **2002**, *73*, 1660.
- (35) Porod, G. In *Small-Angle X-ray Scattering*; Glatter, O.; Kratky, O., Eds.; Academic Press: New York, 1982; p 200.
- (36) Schmidt, P. W. *J. Appl. Crystallogr.* **1991**, *24*, 414.



- (37) Bowden, P. B. In *The Physics of Glassy Polymers*; Haward, R. N., Ed.; John Wiley and Sons: New York, 1973; p 299.
- (38) Ng, C. B.; Ash, B. J.; Schadler, L. S.; Siegel, R. W. *Adv. Compos. Lett.* **2001**, *10*, 101.
- (39) Zhang, J.; Wang, X.; Lu, L.; Li, D.; Yang, X. *J. Appl. Polym. Sci.* **2003**, *87*, 381.
- (40) Sperling, L. H. *Introduction to Physical Polymer Science*; John Wiley and Sons: New York, 2001; p 484.
- (41) Wolock, I.; Kies, J.; Newman, S. In *Fracture: Proceedings of an International Conference on the Atomic Mechanisms of Fracture, April 12–16, 1959*; Averbach, B. L., Felbeck, D. K., Eds.; MIT Press: Boston, MA, 1959.
- (42) Brown, H. R.; Kramer, E. J. *J. Macromol. Sci., Phys.* **1981**, *B19*, 487.
- (43) Reynaud, E.; Jouen, T.; Gauthier, C.; Vigier, G.; Varlet, J. *Polymer* **2001**, *42*, 8759.
- (44) Brandrup, J.; Immergut, E. H.; Grulke, E. A. *Polymer Handbook*, 4th ed.; John Wiley and Sons: New York, 1999.
- (45) Kramer, E. J. *Adv. Polym. Sci.* **1990**, *52*.
- (46) Sternstein, S. S. In *Treatise on Materials Science Technology, Vol. 10, Part, B. Properties of Solid Polymeric Materials*; Schultz, J. M., Ed.; Academic Press: New York, 1977.
- (47) Adams, G. W.; Farris, R. J. *Polymer* **1989**, *60*, 1824.
- (48) Sternstein, S. S. In *Polymeric Materials: Relationships Between Structure and Mechanical Behavior*; American Society for Metals: Metals Park, OH, 1975.
- (49) Nielsen, L.; Landel, R. *Mechanical Properties of Polymers and Composites*; Marcel Dekker Inc.: New York, 1994.
- (50) Gurson, A. L. *Trans. ASME* **1977**, *99*, 2.
- (51) Gent, A. N.; Tomkins, D. A. *J. Polym. Sci., Part A-2* **1969**, *7*, 1483.
- (52) Lazzeri, A.; Bucknall, C. B. *Polymer* **1995**, *36*, 2895.
- (53) van Melick, H. G. H.; Govaert L. E.; Meijer, H. E. H. *Polymer* **2003**, *44*, 457.
- (54) Wu, S. *Polym. Eng. Sci.* **1990**, *30*, 753.
- (55) Chen, L. P.; Yee, A. F.; Goetz, J. M.; Schaefer, J. *Macromolecules* **1998**, *31*, 5371.
- (56) Chen, L. P.; Yee, A. F.; Moskala, E. J. *Macromolecules* **1999**, *32*, 5944.
- (57) Wu, J.; Xiao, C.; Yee, A. F.; Klug, C. A.; Schaefer, J. *J. Polym. Sci., Part B: Polym. Phys.* **2001**, *39*, 1730.

MA0354400